

Hans-Rudolf Kuhn · Detlef Günther

The agglomeration state of nanosecond laser-generated aerosol particles entering the ICP

Received: 16 March 2005 / Revised: 8 July 2005 / Accepted: 11 July 2005 / Published online: 18 August 2005
© Springer-Verlag 2005

Abstract Fundamental understanding of aerosol formation and particle transport are important aspects of understanding and improving laser-ablation ICP–MS. To obtain more information about particles entering the ICP, laser aerosols generated under different ablation conditions were collected on membrane filters. The particles and agglomerates were then visualised using scanning electron microscope (SEM) imaging. To determine variations between different sample matrices, opaque (USGS BCR-2G) and transparent (NIST SRM 610) glass, CaF₂, and brass (MBH B26) samples were ablated using two different laser wavelengths, 193 and 266 nm. This study showed that the condensed nano-particles (~10 nm in diameter) formed by laser ablation reach the ICP as micron-sized agglomerates; this is apparent from filters which contain only a few well-separated particles and particle agglomerates. Ablation experiments on different metals and non-metals show that the structure of the agglomerates is matrix-dependent. Laser aerosols generated from silicates and metals form linear agglomerates whereas particle-agglomerates of ablated CaF₂ have cotton-like structures. Amongst other conditions, this study shows that the absorption characteristics of the sample and the laser wavelength determine the production of micron-sized spherical particles formed by liquid droplet ejection.

Keywords Laser-ablation ICP–MS · Aerosol transport · Particles · Particle agglomeration

Introduction

In laser-ablation inductively coupled plasma mass spectrometry (LA–ICP–MS), laser-generated aerosol particles are vaporised and ionised in an ICP for mass analysis in the

MS [1]. Because particles larger than a critical size (150 nm for glass [2], depending on the ICP instrumentation and conditions) are not completely vaporised, atomised, and transformed into ions, laser conditions must be optimised so that as few large particles as possible are generated, to avoid ICP-induced element-fractionation effects [3–6]. It is, therefore, of major interest to know more about the structure of the particles before they enter the excitation source. Two main particle-formation mechanisms, leading to small and large aerosol particles, respectively, have been reported in literature. These are discussed below.

During laser ablation, a fraction of the ablated sample is described as being vaporised; this condenses in the decreasing laser plasma plume to nanometre-sized particles. Theoretical calculations using condensation and nucleation theories predict particle sizes of a few nanometres [7], tens of nanometres [8] or even hundreds of nanometres [8, 9], depending on the type of background gas and its pressure. Calculations indicate that particles 3 nm in diameter are formed 100 ns after laser impact [10]. Unfortunately, no further information about the transported particle sizes was presented. Particle diameters of several hundred nanometres have been described as very unlikely, however, because an unrealistically large number of atomic collisions would be required for the growing process [11]. In general, the higher rate of collision of gas species at ambient pressure would lead to larger condensed particles than condensation under vacuum conditions [12].

Experimentally, condensed silicon particles between 1 and 10 nm, generated by a KrF laser and deposited on TEM grids, have been measured under vacuum conditions [13]. Other authors reported glass particles with maximum diameters between 20 and 50 nm [14] when using a 351-nm XeF laser in a vacuum, depending on the laser energy. Most nanometre-sized particles have been measured as agglomerates on TEM grids, but it has not been reported where the agglomeration occurs. Agglomeration is, however, very likely as soon as the particle number density exceeds a certain value [13]. The particle number density reaches its maximum immediately after condensation and before dilution with the carrier gas. When

H.-R. Kuhn · D. Günther (✉)
ETH Zurich, Laboratory for Inorganic Chemistry,
8093 Zurich, Switzerland
e-mail: guenther@inorg.chem.ethz.ch
Fax: +41-44-6331071

agglomerates are formed it is therefore feasible that agglomeration starts within the ablation cell immediately after particle formation.

The second mechanism described for particle generation is direct ejection of droplets from the molten sample surface. This is affected by interactive conditions such as laser wavelength, sample absorption [15], and irradiation [16]. At low power densities ($<22 \text{ GW cm}^{-2}$ for silicon), but above the ablation threshold, laser-induced photomechanical stress leads to ejection of droplets which are up to several microns in diameter [12]. The size and amount of these particles are strongly affected by mechanical and surface properties of the sample. At higher power densities ($>22 \text{ GW cm}^{-2}$ for silicon), phase explosion or explosive boiling of the molten sample leads to ejection of large particles from the sample [16–18]. On filter-collected aerosol particles of lead, steel, glass, and ceramics [19–21] it has been shown that much of the ablated mass is transported as micron-sized spherical particles. Particle-size measurements using different laser wavelengths [22] indicate that the particle-size distribution strongly depends on the wavelength when ablating glass samples.

Particle-size distributions of laser-generated brass aerosols have been measured using laser-light scattering or particle impaction [6, 23]. Recent studies comparing the aerosols produced by nanosecond and femtosecond laser ablation reported agglomerated nano-particles and single particles up to 200 nm for femtosecond laser pulses [24] whereas particles up to several microns were observed for 266-nm nanosecond laser ablation [23, 24]. The SEM image of the largest particle ($>2 \mu\text{m}$) was, however, of insufficient resolution for structural conclusions and could also represent agglomerated particles. Furthermore, particles were collected on a silicon surface [24] acting as an impaction plate, and so might not be representative for the overall transported aerosol.

The two mechanisms discussed lead to two mainly independent particle size distributions based on condensed nano-particles or on ejected, solidified droplets. All types of particles are present within the same aerosol.

This study investigated the particle size and structure of the laser-generated aerosols routinely used in LA–ICP–MS, and their dependence on sample matrix, laser wavelength, and carrier gas composition. Another objective was to determine the state of agglomeration of the particles during transport before they enter the ICP. The presence of agglomerates would affect the various techniques used for particle-size determination. Because diffusion losses are more pronounced for very small particles, agglomeration of these particles would enhance the efficiency of transport of the aerosol particles [23].

Experimental

Laser ablation instrumentation

The aerosols investigated were generated using two different laser wavelengths. All experiments were performed

using a beam-homogenised 193 nm ArF excimer laser [25] (GeoLas M, MicroLas, Göttingen, Germany) and a 266-nm 4th harmonics Nd:YAG laser (LSX500, Cetac Technologies, Omaha, NE, USA). Power density and spot size were set to 2 GW cm^{-2} and $80 \mu\text{m}$ for the 193 nm laser and to 2 GW cm^{-2} and $100 \mu\text{m}$ for the 266 nm laser, respectively (Table 1). Both lasers were operated at a repetition rate of 5 Hz and at power densities similar to those commonly used for LA–ICP–MS.

The samples were placed in a 30 cm^3 ablation cell, which was flushed with 0.4 L min^{-1} carrier gas. For most experiments, helium was selected as the carrier gas; this resulted in higher sensitivity for many ICP–MS instruments for silicate matrices [26, 27], because of the enhanced aerosol transport characteristics [6, 23]. Glass aerosols generated under argon atmosphere were also investigated, however, to determine possible variations of the aerosol characteristics. All samples were ablated in the single-hole drilling mode.

Particle filtering procedure

The filter was placed 0.5 m downstream of the ablation cell to collect the aerosol particles. The requirements for the filter material were a flat surface to ensure good visibility of the particles by scanning electron microscopy (SEM) and sufficient gas permeability to minimize carrier gas backpressure in the ablation cell. Membrane filters with a pore size of 400 nm were found to be suitable for the experiments (Isopore Membrane Filters HTTP01300, Millipore, Billerica, MA, USA). Most important, mounting of this type of filter on a conductive carbon tape enables SEM measurements without conductive surface coating. The ICP–MS signal intensities measured online were reduced by more than five orders of magnitude when inserting the filter between ablation cell and the ICP, indicating that most of the aerosol particles were deposited on the filter.

To obtain bulk information about particle sizes, 100 laser pulses were applied. For more detailed particle structures, five laser pulses only were applied to the sample resulting in well-separated particles on the filter surface. Previously published work showed that the amount of small particles remains constant during the first 100 laser pulses [2]. The amount of micron-sized particles decreases significantly within this time period, however, and, therefore, these particles are expected to be more numerous than the small particles when applying only five laser pulses.

Table 1 Experimental conditions

Laser	193 nm (15 ns pulse length), 266 nm (6 ns pulse length)
Power density	2 GW cm^{-2} for both lasers
Carrier gas	He (normal) or Ar (indicated)
Gas flow rate	0.4 L min^{-1}
Samples	NIST SRM 610, USGS BCR-2G, Fluorite, B26 brass

SEM images were collected at the microscopy centre at ETH Zurich with a Zeiss Gemini 1530 FEG instrument (Carl Zeiss, Germany) using a zirconated tungsten emitter and secondary electron detection (SE+ detector). A low acceleration voltage of 1 kV was used to reduce surface charging effects, which slightly reduced image resolution.

Samples

A NIST (National Institute of Standards and Technology, USA) standard reference material (SRM) 610 glass was selected as a sample for this study, because it is one of the calibration standards most frequently used for quantitative analysis in LA-ICP-MS [1]. The aerosol particle structure of this material is therefore of particular interest. Other matrices including metals and non-metals were also investigated. Fluorite (CaF_2) was selected because of its low absorptivity and was compared with the high-absorbing USGS BCR-2G (Columbia River Basalt, US Geological Survey, USA) basaltic glass standard [28]. A brass sample (B26, MBH Analytical, UK; Cu/Zn=2.10) was selected as a metal sample. All non-metals were pre-ablated with five laser pulses, because these pulses have been shown to be not representative for chemical analysis [29].

Results and discussion

Aerosol structure of NIST SRM 610 after laser ablation

An experiment was designed to gain an overview of an NIST SRM 610 aerosol generated by using two different laser wavelengths. Particles from 100 ablation pulses were collected on filters to determine the overall size and shape of the aerosol particles. The particles were not fully randomly distributed on the filter surface, possibly because of variation of the gas permeability of the filter surface. The absolute particle numbers and the particle size-related mass could not, therefore, be directly correlated with the number of laser pulses. Despite this, the images shown in Fig. 1 provide evidence of two fundamentally different particle-generation mechanisms. For both laser wavelengths, a grid-like structure of particles smaller than approximately 10 nm was observed on the filter surface. Condensation from the vapour phase is the most probable origin of these particles. Ten nanometres is in the low region of the size range expected for vapour-condensed particles [7–14]. In addition to condensed vapour, direct ejection of droplets has been predicted and shown in literature to be a second mechanism of aerosol generation during laser ablation [16–21]. Such solidified droplets are transported in the aerosol together with the smaller condensed particles and

Fig. 1 Filtered aerosol of NIST SRM 610 glass after 100 ablation pulses. **a, b**) 266 nm laser, 100 μm spot size. Large particles and agglomerates of nano-particles are visible. **c, d**) 193 nm laser, 80 μm spot size. Almost exclusively agglomerates of nano-particles are visible; no spherical particles are larger than 200 nm. The pores of the filter are visible in the images as dark areas

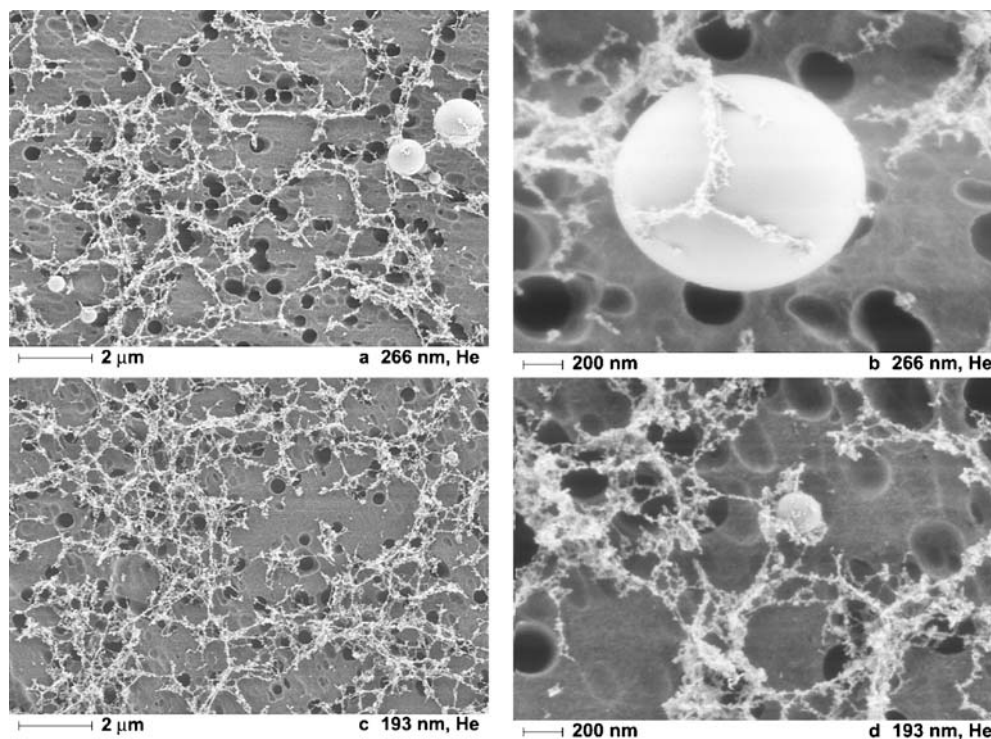
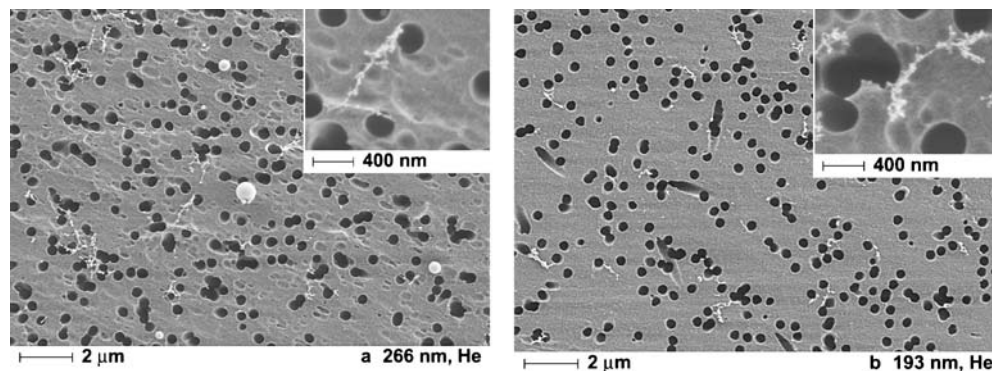


Fig. 2 Filtered aerosol of NIST SRM 610 glass after five laser pulses showing well separated particles and agglomerates.

a Particles and agglomerates generated by 266 nm laser ablation (100 μm spot size). **b** Agglomerates generated using 193 nm laser ablation (80 μm spot size). The pores of the filter are visible in the images as dark areas



are visible on the filters (Fig. 1a and b) depicting the aerosol generated using 266-nm laser ablation. The aerosol contains significant amounts of spherical particles in a size range of up to 2 μm , no significant agglomeration of these spherical particles was observed. In contrast, the aerosol from 193-nm laser ablation (Fig. 1c and d) contains no spherical particles exceeding 250 nm in size (Fig. 1d). These round-shaped 250 nm particles were also found to be extremely rare. The main part of the aerosol produced by the 193 nm laser consists of agglomerates of primary particles generated by vapour condensation.

Agglomeration of condensed nano-particles

Because the agglomerated particles shown in Fig. 1 do not enable determination of the origin of agglomeration and it remains questionable whether the condensed particles are transported as agglomerates immediately formed after the ablation or whether agglomeration occurs on the filter itself during particle deposition, only five laser pulses were applied to the sample to increase the distance between the deposited particles on the filter. Figure 2a (266 nm) and b (193 nm) show almost “clean” filters containing only a few well-separated, spherical particles and agglomerates of nano-particles. Again, the observations for 266 nm and 193 nm laser ablation (Fig. 1), showing that large particles are formed at 266 nm, are also confirmed for the low number of laser pulses. The agglomerates, however, seem comparable in size (approximately 0.5–2 μm) and are similar in structure for both wavelengths. This observation is a strong indication that a significant amount of the

ablated material undergoes the same fundamental process of condensation for both laser wavelengths. It can be assumed that the particle number density of condensed particles is high enough for agglomeration within the laser-induced plasma or during transport of the aerosol.

Figure 1b shows that the large, spherical aerosol particles generated at 266 nm have a smooth, unstructured surface. Agglomerates attached to the particle surface (Fig. 1b) and single agglomerates (Fig. 2b) are similarly shaped and are, apparently, captured by the spherical particle during aerosol transport or on the filter after deposition.

To assign the formation of the agglomerates to the ablation cell or the aerosol transport, particles were generated under stopped-gas-flow conditions within the ablation cell using approximately 100 laser pulses at 193 nm. The particles were then flushed to the filter. Agglomerates generated at a longer residence time within the ablation cell were expected to be larger, because of the continuously growing aerosol particle number density in the ablation cell. The shapes of the filter-collected agglomerates generated under stopped-gas-flow conditions (Fig. 3b) are significantly different from those of the agglomerates formed under normal gas flow (Fig. 3a). Larger and more compact agglomerates are formed under stopped-gas-flow conditions whereas particles agglomerated under constant gas flow show more grid-like structures as already shown in Fig. 1c. This is another indication that particle agglomeration occurs within the ablation cell and is not a result of the filter collection process. Further experiments with carrier gas flow rates between 0.1 and 1 L min^{-1} gave no further indication of a change in the size of the ag-

Fig. 3 a Filter-collected aerosol particles after 100 laser pulses (193 nm) transported using continuous gas flow. b)

Agglomerates generated by approximately 100 pulses under stopped-gas-flow conditions, subsequently flushed to the filter. The pores of the filter are visible in the images as dark areas

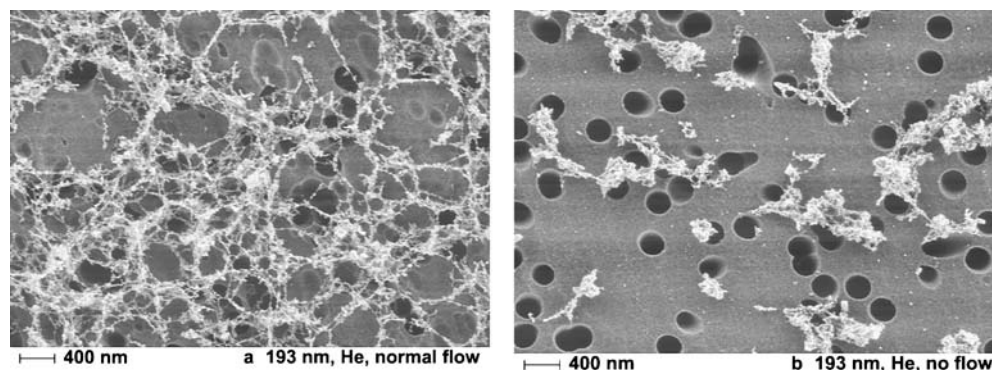
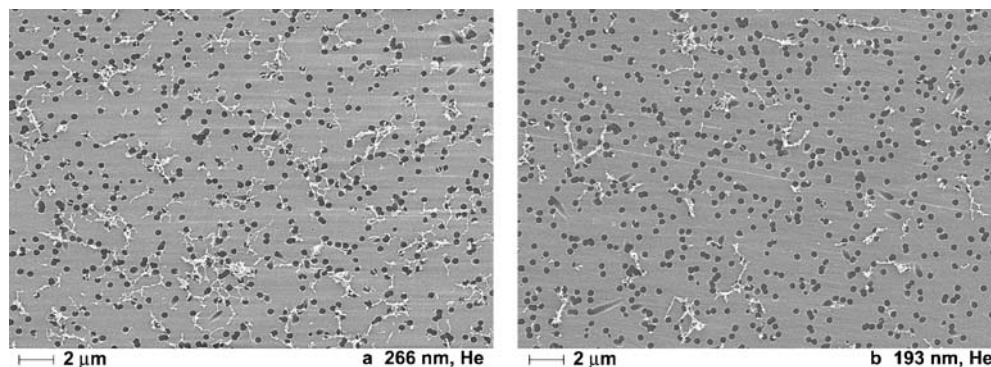


Fig. 4 Filtered aerosol from a BCR-2G basaltic glass after 100 laser pulses. **a** 266 nm. **b** 193 nm. In contrast with NIST SRM 610, no spherical particles are visible for both wavelengths. However, the shape of the agglomerates is comparable with those from NIST SRM 610, because of the similar silicate matrix. The pores of the filter are visible in the images as dark areas



glomerates. The fact that aerosol dilution does not affect aerosol particle sizes supports the finding that the agglomerates are formed immediately after condensation of their primary nano-particles is complete.

Aerosol structure of opaque BCR-2G basaltic glass

Particle formation for NIST SRM 610 glass and the opaque BCR-2G reference material was compared using 266 nm and 193 nm ablation for aerosol generation. Figure 4 shows the particles collected from ablated BCR-2G. Filter-collected agglomerates of nano-particles reveal no significant differences between sizes and shapes for the two ablation conditions. The shapes of the agglomerates are similar, because both materials consist of a silicate matrix and differ mainly in their optical properties. The absorptivity determines the penetration depth in BCR-2G, which is small enough for both wavelengths to achieve complete vapour transition of the ablated sample material. Therefore, larger particles are absent for this high-absorbing glass. Such exclusive vapour condensation and agglomeration can usually be assumed for high-absorbing non-metal samples at the power densities used in these experiments.

Comparison of the particle structures of NIST SRM 610 and BCR-2G leads to some general conclusions relevant to quantification using LA-ICP-MS, e.g. quantification of highly absorbing samples by using transparent NIST SRM 610 as an SRM at 266 nm is not as suitable as at 193 nm, because of the significantly different particle-size distribution generated by laser ablation. Furthermore, and as pre-

viously shown, the elemental composition of the aerosol particles depends on the particle size [30]. Therefore, differences between the particle structure observed at 266 nm for NIST SRM 610 and BCR-2G can lead to matrix effects within the ICP, because of incomplete particle vaporisation. Matching of the absorptivity for 266 nm of sample and calibration standard will, however, result in aerosol particles of similar sizes and is, therefore, preferable for more accurate quantitative analysis in LA-ICP-MS, although the micron-sized spherical particles disturb the ICP substantially and lead to higher RSDs.

Transparent fluorite (CaF_2)

Pure fluorite is one of the most transparent materials in the low UV range. Because it has been shown for the NIST SRM 61X standard glass series that more large, spherical particles in the micron range are generated in the order $266 \text{ nm} > 213 \text{ nm} > 193 \text{ nm}$ [15], an increased presence of these particles was also expected for the more transparent CaF_2 . Figure 5a shows that even 193 nm ablation produces significant amounts of particles approximately $0.5 \mu\text{m}$ in diameter that are deposited on the filter. However, spherical particles up to $2 \mu\text{m}$ in diameter were detected on the filter. Besides these micron-sized particles, the shapes of the agglomerates deposited on the filter were different from those of the agglomerates produced from the silicate glass samples (Figs. 1–4). Whereas the agglomerates from ablated silicates were more linear in structure, the agglomerates from CaF_2 were larger and had a cotton-like structure

Fig. 5 Filtered aerosol of transparent CaF_2 ablated with a 193 nm laser at $80 \mu\text{m}$ spot size. **a** 100 ablation pulses; **b** five ablation pulses. Spherical particles and cotton-like structured agglomerates are formed. The pores of the filter are visible in the images as dark areas

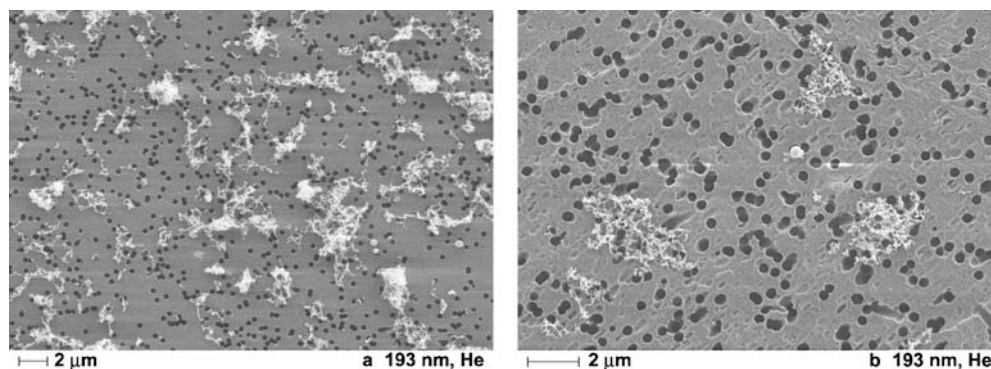
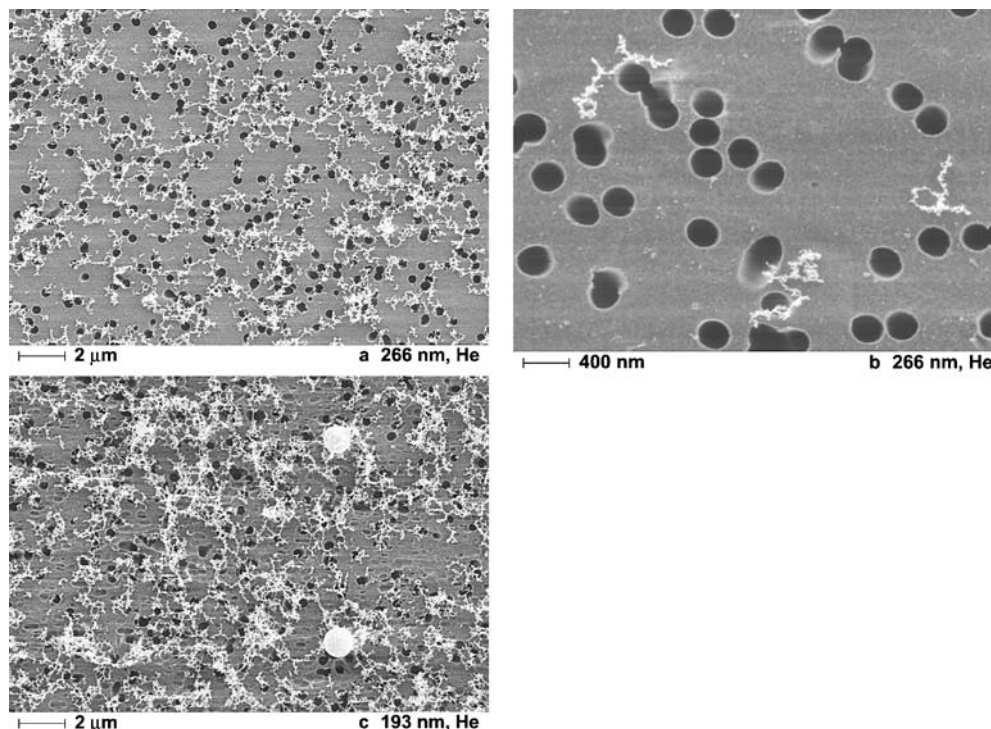


Fig. 6 **a** Filtered aerosol obtained from brass (B26) after 266 nm ablation at 2 GW cm^{-2} (100 pulses). Under these conditions, no large particles are generated. **b** After five pulses, well-separated agglomerates are deposited on the filter. **c** During 193 nm ablation at 2 GW cm^{-2} spherical particles and agglomerates are generated. The pores of the filter are visible in the images as dark areas



(Fig. 5b). This indicates that for each sample matrix, different shaped agglomerates must be expected.

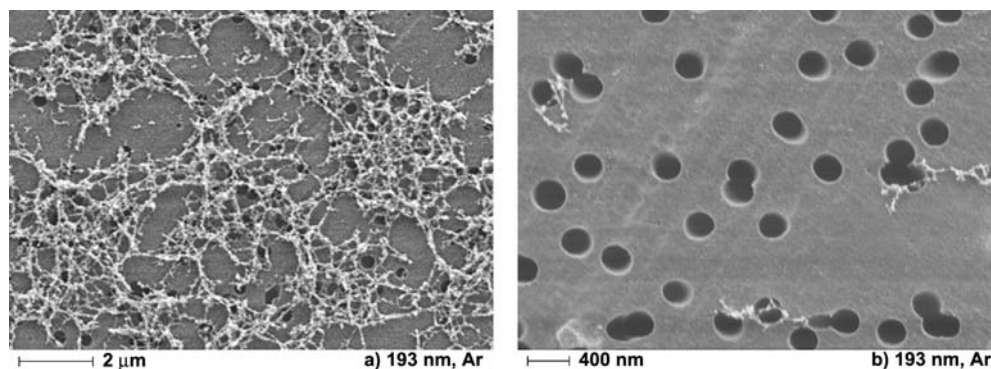
It is, therefore, important to mention that in a filter-influenced agglomeration process such matrix-dependent agglomeration structures would be difficult to explain.

Brass sample

The SEM images obtained from laser-generated and filter-collected brass aerosols indicate that vapour condensation is the predominant particle-formation mechanism for nano-second laser ablation at 266 nm (Fig. 6a) and 193 nm (Fig. 6c). Figure 6b shows the almost fractal-structured agglomerates of nano-particles, which are comparable in shape for both laser wavelengths. A variable amount of micron-sized, spherical particles is transported together with condensed vapour, depending on the laser operating

conditions selected. At 266 nm and power densities of 0.25 and 2 GW cm^{-2} almost exclusively condensed and agglomerated particles are generated, whereas power densities in between (0.75 and 1.3 GW cm^{-2}) lead to agglomerates and spherical particles in the micron range. A similar effect was measured for 193 nm laser ablation; at lower power densities ($<0.3 \text{ GW cm}^{-2}$) exclusively vapour is generated. No upper power density limit for complete vapour transition of the sample was measured at 193 nm and 2 GW cm^{-2} , however. With regard to the vaporisation and ionisation of the aerosol particles in the ICP, laser energies leading to small particles or agglomerates are preferable for LA-ICP-MS. Different studies have reported non-stoichiometric aerosol compositions at low laser energies [23, 31, 32], however, and that two sources of elemental fractionation can be observed (laser-induced and ICP-induced). High power densities at 266 nm also leading to exclusively small aerosol particles are therefore preferable

Fig. 7 Filtered aerosol of NIST SRM 610 glass generated by 193 nm laser ablation in argon atmosphere after 500 shots (a) and after five shots (b) at $80 \mu\text{m}$ spot size. The amount of particles on the filter after 500 shots in argon (a) is comparable with that in helium after 100 shots only (Fig. 1c), indicating that the transport efficiency in argon is significantly lower. The pores of the filter are visible in the images as dark areas



for quantitative analysis. More accurate results were also reported from femtosecond laser ablation [23] indicating that, for metals, the pulse length is an important condition.

Differences between argon and helium carrier gas

NIST SRM 610 was ablated at 193 nm using argon and helium as ambient gas during the ablation and as carrier gases. Previous particle-size-distribution measurements [33] indicated that the carrier gas shifts the particle size distribution towards smaller particles when using helium instead of argon. Furthermore, a 3–5 fold ICP–MS signal increase has been reported for 193 nm when using helium as carrier gas [26]. Both observations were made on the NIST SRM 610 glass.

When the particles deposited on the filter after a constant number of laser pulses are compared for both carrier gases it becomes obvious that the amount of deposited material after 500 laser pulses in argon (Fig. 7a) is comparable with that deposited after 100 pulses in helium (Fig. 1c). When considering the similar ablation rates of the laser for the two carrier gas environments [34], this indicates that use of helium significantly enhances the transport efficiency. The lower transport efficiency in argon is accompanied by greater deposition of particles on the sample surface [33]. The size and shape of the deposited particles seem to be independent of carrier gas properties (Fig. 7b). The resolution of the SEM is incapable of resolving changes in the size of primary particles below 10 nm, which might exist. However, a changed particle size within the low-nanometre range is not expected to change the vaporization behaviour in the ICP.

Conclusions

For laser ablation, two particle-formation mechanisms have been described in the literature; these lead to condensed nano-particles and to micron-sized spherical particles. Both types of particles were confirmed in this study of aerosol particles collected on filters before entering the ICP.

The SEM images shown here reveal vapour-condensed particles in the 10 nm range for different sample matrices such as glass, fluorite or metals. Furthermore and most important, these particles are transported as micron-sized agglomerates by the carrier gas and are most probably formed within the ablation cell. This result has a significant effect on the aerosol-measurement procedures as applied in Refs. [2, 23, 35]. It enables, for example, particle sizing with optical light scattering, which would not be possible for the primary 10 nm particles because light-scattering intensities would be too low. Furthermore, the agglomerates are too large to be separated by diffusion separation techniques. This is possible only for particles with physical dimensions smaller than approximately 200 nm—larger particles cannot be selectively separated by this technique.

This study shows also that the shape of the agglomerates depends on the ablated sample matrix, and is indepen-

dent of the laser wavelength. The laser wavelength and sample absorptivity do, however, determine the amount of micron-sized spherical particles generated from non-metal samples. For non-metal samples, fewer of these particles are present in aerosols generated at 193 nm compared to 266 nm ablation or for opaque samples such as BCR-2G.

Metals readily absorb different laser wavelengths with comparable efficiencies, but their high thermal conductivity increases the molten volume of the sample, especially for samples with low melting points, and can lead to enhanced splashing of large droplets. Reduction of droplet ejection by reducing the energy of the laser is critical, because non-stoichiometric aerosols can be produced. Stoichiometric composition is, however, expected to be better for aerosols from high-energy ablation of brass leading to exclusively vapour generation. No data are available, however, and determination of elemental composition will be part of further investigation.

Comparison of the effect of using argon and helium carrier gas shows no difference between particle or agglomerate structures. The total amount of particles transported by helium is, however, significantly higher.

The results of this work reveal a need for more critical evaluation of the techniques used for particle-size distribution measurements, because of the simultaneous presence of spherical particles and agglomerates of similar particle diameters within the aerosol. For glass samples with different transparencies, it can be concluded that aerosol structures are more similar after laser ablation at 193 nm than after ablation at 266 nm.

Acknowledgements This work was funded by the ETH Zurich and the Swiss National Science Foundation. The support by Dr Frank Krumeich and Michael Stalder, who facilitated the SEM measurements, is greatly appreciated.

References

- Russo RE, Mao XL, Liu HC, Gonzalez J, Mao SS (2002) *Talanta* 57:425–451
- Kuhn HR, Guillong M, Günther D (2004) *Anal Bioanal Chem* 378:1069–1074
- Stirling CH, Lee DC, Christensen JN, Halliday AN (2000) *Geochim Cosmochim Acta* 64:3737–3750
- Figg D, Kahr MS (1997) *Appl Spectrosc* 51:1185–1192
- Guillong M, Günther D (2002) *J Anal At Spectrom* 17:831–837
- Kuhn HR, Günther D (2003) *Anal Chem* 75:747–753
- Callies G, Schittenhelm H, Berger P, Hugel H (1998) *Appl Surf Sci* 129:134–141
- Kar A, Mazumder J (1994) *Phys Rev E* 49:410–419
- Gnedovets AG, Gusarov AV, Smurov I (2000) *Appl Surf Sci* 154:508–513
- Bogaerts A (2004) Can modeling help us to “See the light”? Conference on Plasma Spectrochemistry, Fort Lauderdale, FL
- Bogaerts A, Chen ZY, Gijbels R, Vertes A (2003) *Spectrochim Acta Part B* 58:1867–1893
- Zhigilei LV (2003) *Appl Phys A-Mater Sci Process* 76:339–350
- Geohegan DB, Poretzky AA, Duscher G, Pennycook SJ (1998) *Appl Phys Lett* 72:2987–2989
- Zheng J, Lou QH, Dong JX, Li J, Wei JR (1996) *Opt Commun* 132:285–288

15. Guillong M, Horn I, Günther D (2003) *J Anal At Spectrom* 18:1224–1230
16. Yoo JH, Jeong SH, Mao XL, Greif R, Russo RE (2000) *Appl Phys Lett* 76:783–785
17. Yoo JH, Jeong SH, Greif R, Russo RE (2000) *J Appl Phys* 88:1638–1649
18. Lu QM, Mao SS, Mao XL, Russo RE (2002) *Appl Phys Lett* 80:3072–3074
19. Huang Y, Shibata Y, Morita M (1993) *Anal Chem* 65:2999–3003
20. Baker SA, Smith BW, Winefordner JD (1998) *Appl Spectrosc* 52:154–160
21. Thompson M, Chenery S, Brett L (1990) *J Anal At Spectrom* 5:49–55
22. Alexander ML, Smith MR, Hartman JS, Mendoza A, Koppelaar DW (1998) *Appl Surf Sci* 129:255–261
23. Koch J, von Bohlen A, Hergenröder R, Niemax K (2004) *J Anal At Spectrom* 19:267–272
24. Liu C, Mao XL, Mao SS, Zeng X, Greif R, Russo RE (2004) *Anal Chem* 76:379–383
25. Günther D, Frischknecht R, Heinrich CA, Kahlert HJ (1997) *J Anal At Spectrom* 12:939–944
26. Egdins SM, Kinsley LPJ, Shelley JMG (1998) *Appl Surf Sci* 129:278–286
27. Günther D, Heinrich CA (1999) *J Anal At Spectrom* 14:1363–1368
28. Gao S, Liu XM, Yuan HL, Hattendorf B, Günther D, Chen L, Hu SH (2002) *Geostand News* 26:181–196
29. Jeong SH, Borisov OV, Yoo JH, Mao XL, Russo AE (1999) *Anal Chem* 71:5123–5130
30. Kuhn HR, Günther D (2004) *J Anal At Spectrom* 19:1158–1164
31. Mao XL, Ciocan AC, Russo RE (1998) *Appl Spectrosc* 52:913–918
32. Mao XL, Chan WT, Caetano M, Shannon MA, Russo RE (1996) *Appl Surf Sci* 96(8):126–130
33. Horn I, Günther D (2003) *Appl Surf Sci* 207:144–157
34. Horn I, Guillong M, Günther D (2001) *Appl Surf Sci* 182:91–102
35. Kosler J, Wiedenbeck M, Wirth R, Hovorka J, Sylvester P, Mikova J (2005) *J Anal At Spectrom* 20:402–409